Supplementary Information (SI) for Sustainable Energy & Fuels.
This journal is © The Royal Society of Chemistry 2025

Electronic Supplementary Information

Chemically Pre-Lithiated/Sodiated Reduced Graphene Oxide-Antimony Oxide Composites for High-Rate Capability and Long-Term Cycling Stability in Lithium and Sodium-Ion Batteries

*Minseop Lee[a]‡, Gi-Chan Kim[a]‡, and Seung-Min Paek[a]**

[a]Department of Chemistry, Kyungpook National University, Daegu 41566, Republic of Korea

*E-mail: smpaek@knu.ac.kr

‡These authors contributed equally.

Supplementary Figs. and Tables.

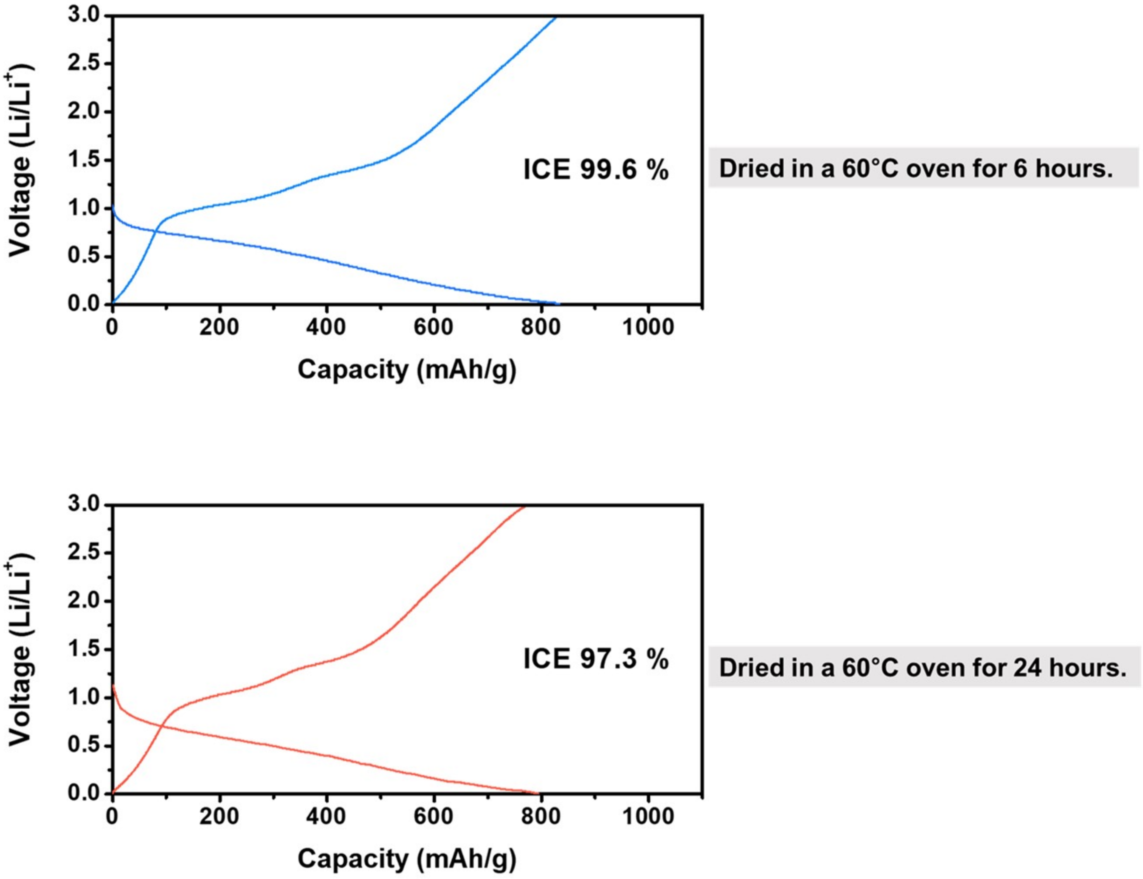

Fig. S1. Comparison of initial coulombic efficiency (ICE) of PL-MrGO/$Li_xSb_2O_3$ electrodes dried at 60°C for different drying times (6 and 24 hours).

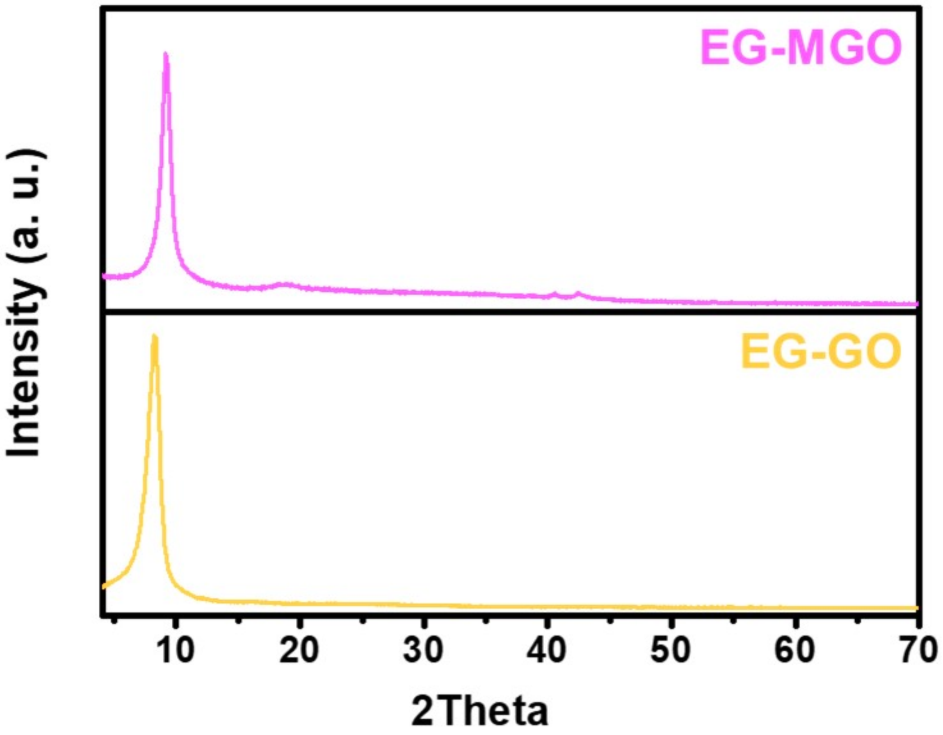

Fig. S2. XRD patterns for EG-GO and EG-MGO.

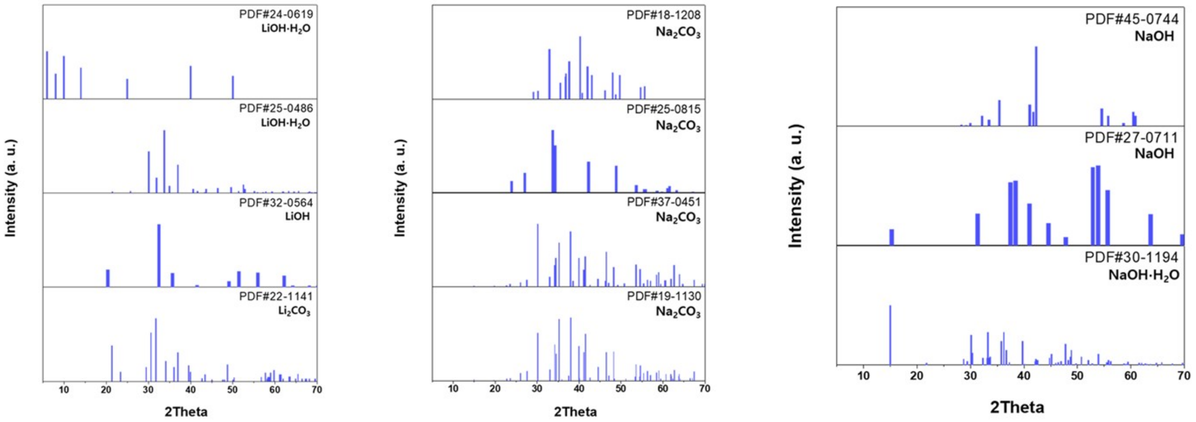

Fig. S3. XRD spectra of Li(Na)OH or Li(Na)$_2$CO$_3$, as identified from the PDF card (Database).

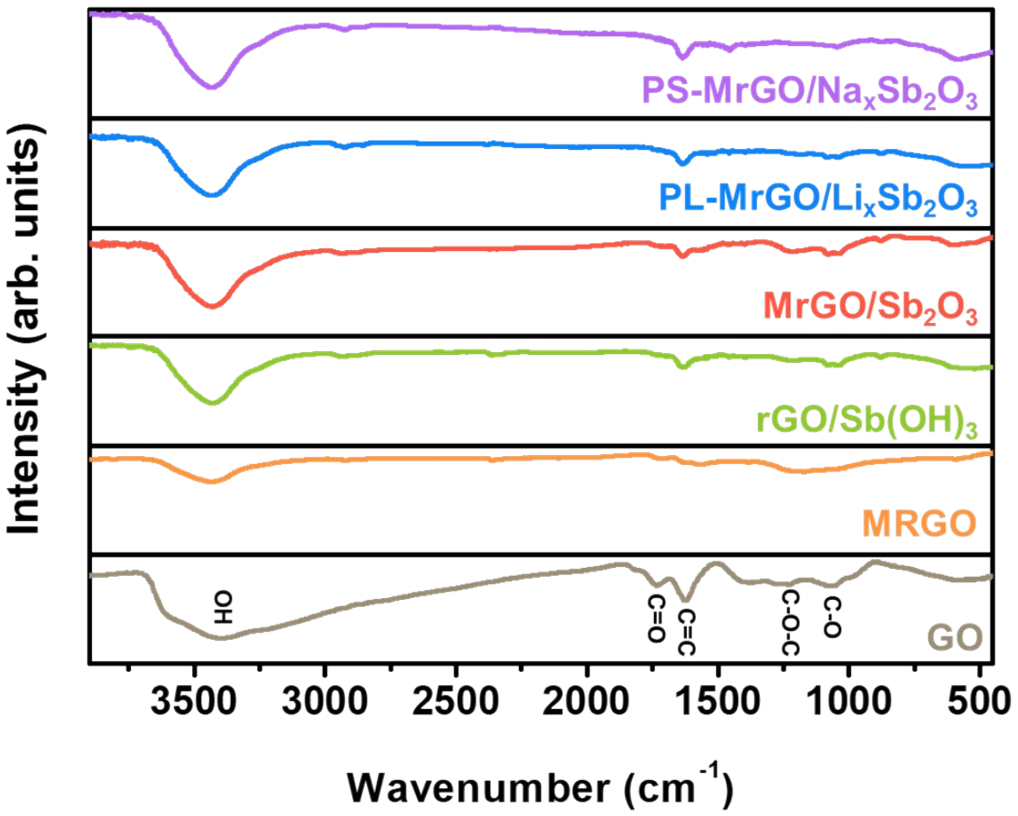

Fig. S4. FTIR spectra of GO, MrGO, rGO/Sb(OH)$_3$, MrGO/Sb$_2$O$_3$, PL-MrGO/Li$_x$Sb$_2$O$_3$, and PS-MrGO/Na$_x$Sb$_2$O$_3$.

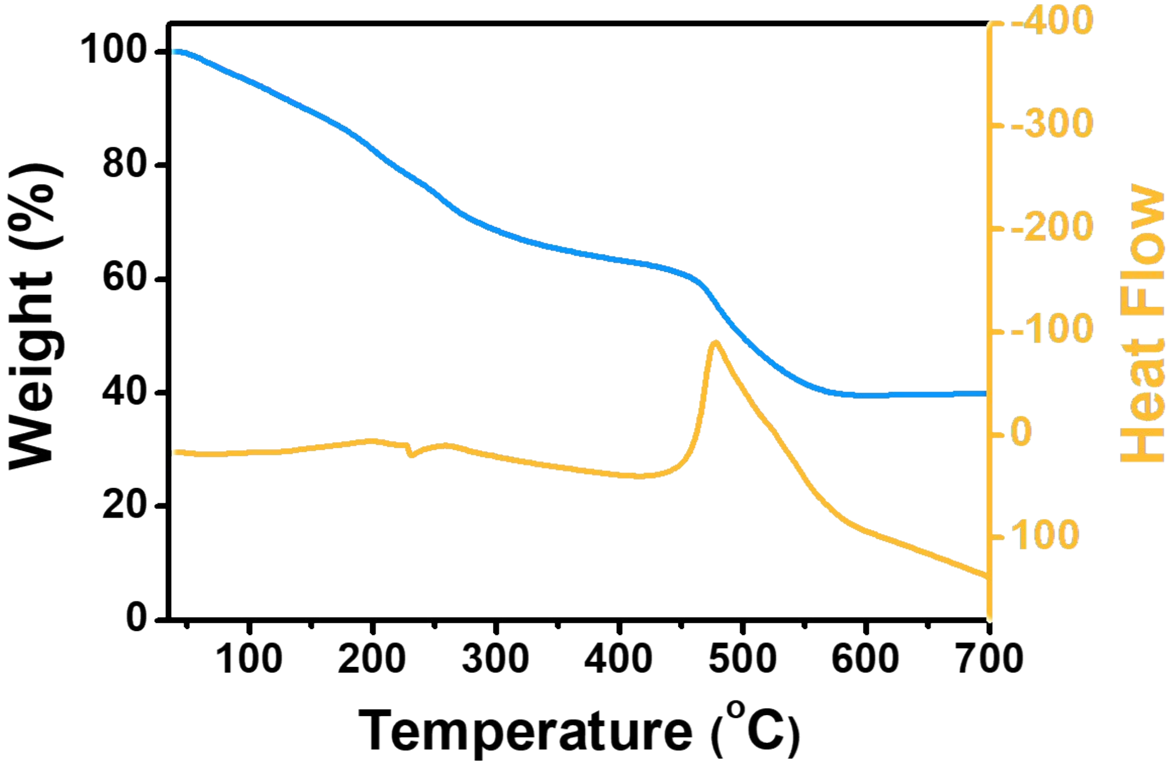

Fig. S5. TGA profiles performed in an ambient atmosphere of MrGO/Sb_2O_3.

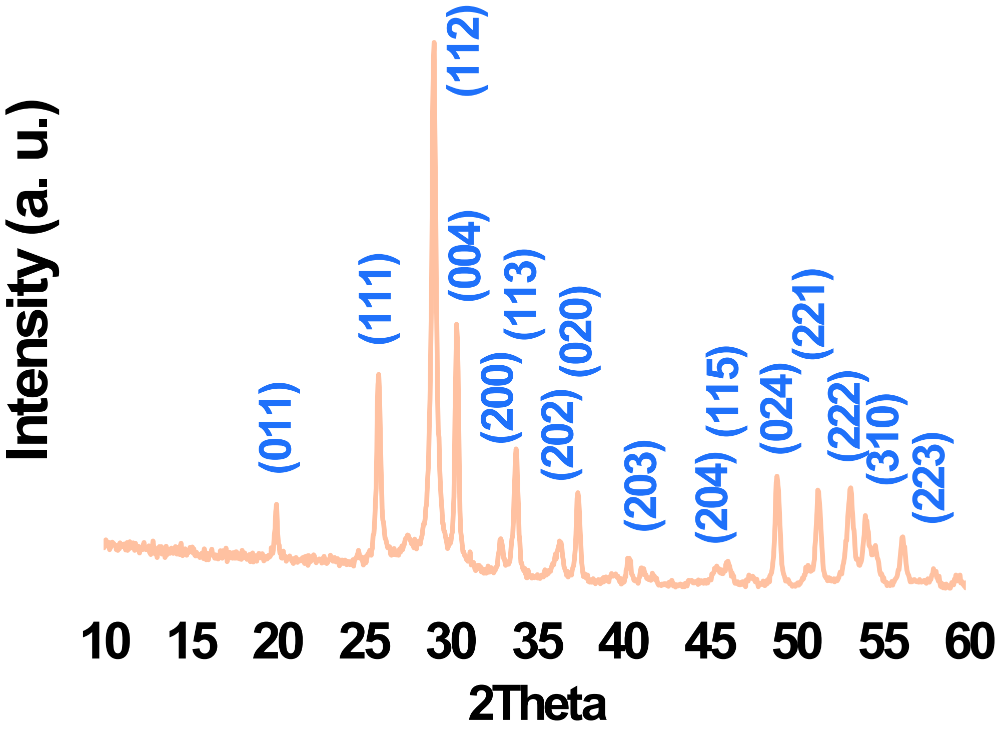

Fig. S6. XRD patterns of the residue after a TGA scan of MrGO/Sb_2O_3.

Table S1. TGA, ICP, XPS, and TEM-EDS elemental analysis results of MrGO/Sb_2O_3.

TGA (wt%)	**ICP (wt%)**	**EDS (wt%)**	**XPS (wt%)**		
$^{a}Sb_2O_4$	**^{b}Sb**	**^{c}Sb**	**C**	**O**	**^{d}Sb**
39.50	**29.81**	**27.23**	**52.45**	**15.25**	**32.30**

$^{a}Sb_2O_4$ residual mass = 39.50 wt%, Sb = 31.28 wt%, Sb_2O_3 = 37.44 wt% (In the MrGO/Sb_2O_3)

^{b}Sb componenet = 29.81 wt%, Sb_2O_3 = 35.68 wt% (In the MrGO/Sb_2O_3)

^{c}Sb componenet = 27.23 wt%, Sb_2O_3 = 32.59 wt% (In the MrGO/Sb_2O_3)

^{d}Sb componenet = 32.30 wt%, Sb_2O_3 = 38.66 wt% (On the MrGO/Sb_2O_3 surface)

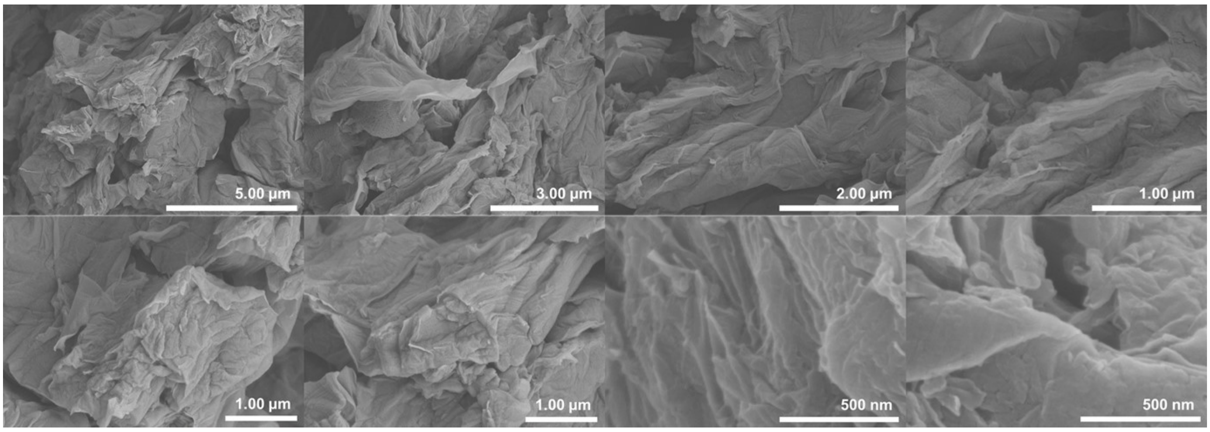

Fig. S7. SEM images of GO.

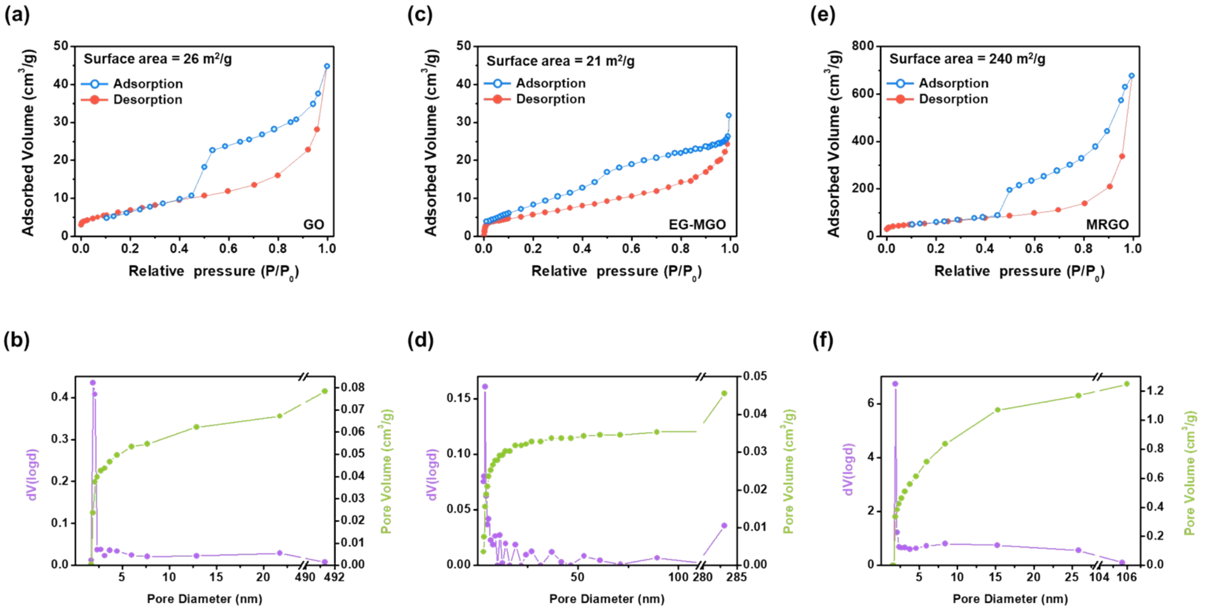

Fig. S8. N_2 adsorption-desorption isotherms and pore size distribution curve based on the Barrett-Joyner-Halenda (BJH) method for (a,b) GO, (c,d) EG-MGO, and (e,f) MrGO.

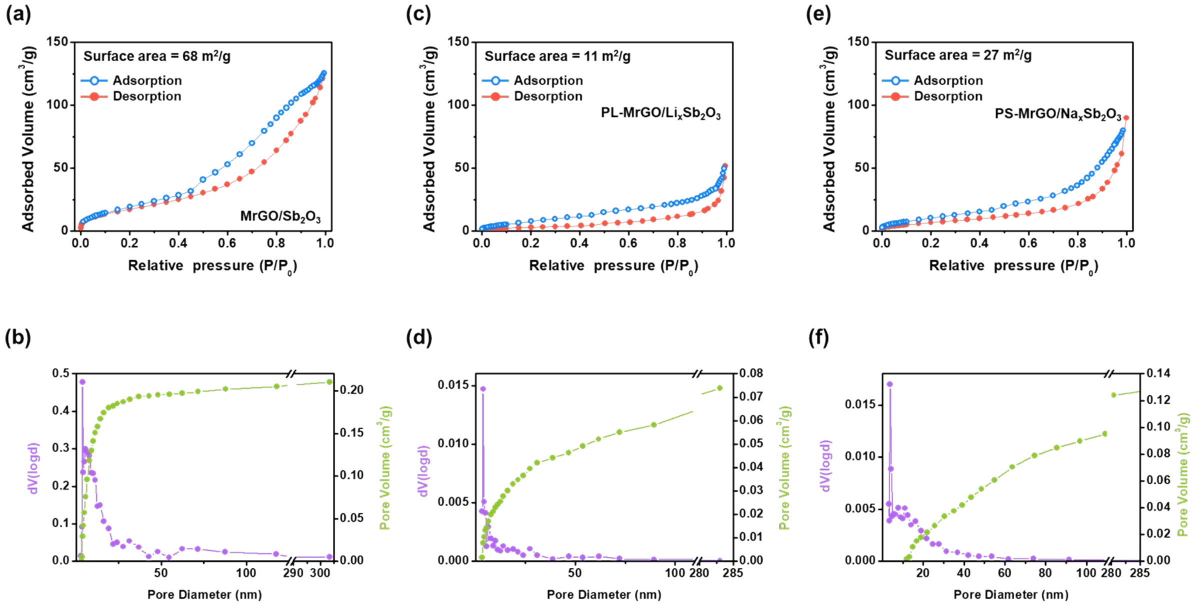

Fig. S9. N_2 adsorption-desorption isotherms and pore size distribution curve based on the Barrett-Joyner-Halenda (BJH) method for (a,b) MrGO/Sb_2O_3, (c,d) PL-MrGO/$Li_xSb_2O_3$, and (e,f) PS-MrGO/$Na_xSb_2O_3$.

Table S2. Surface area, pore volume, and pore diameter corresponding to **Figs. S12** and **S13**.

	Surface area (m^2g^{-1}), BET method	**Pore volume (cm^3g^{-1}), BJH method des**	**Pore diameter (nm), BJH method des**
GO	26	0.078	1.91
EG-MGO	21	0.046	3.83
MrGO	240	1.25	1.91
MrGO/Sb_2O_3	68	0.21	3.82
PL-MrGO/$Li_xSb_2O_3$	11	0.074	3.81
PS-MrGO/$Na_xSb_2O_3$	27	0.14	3.84

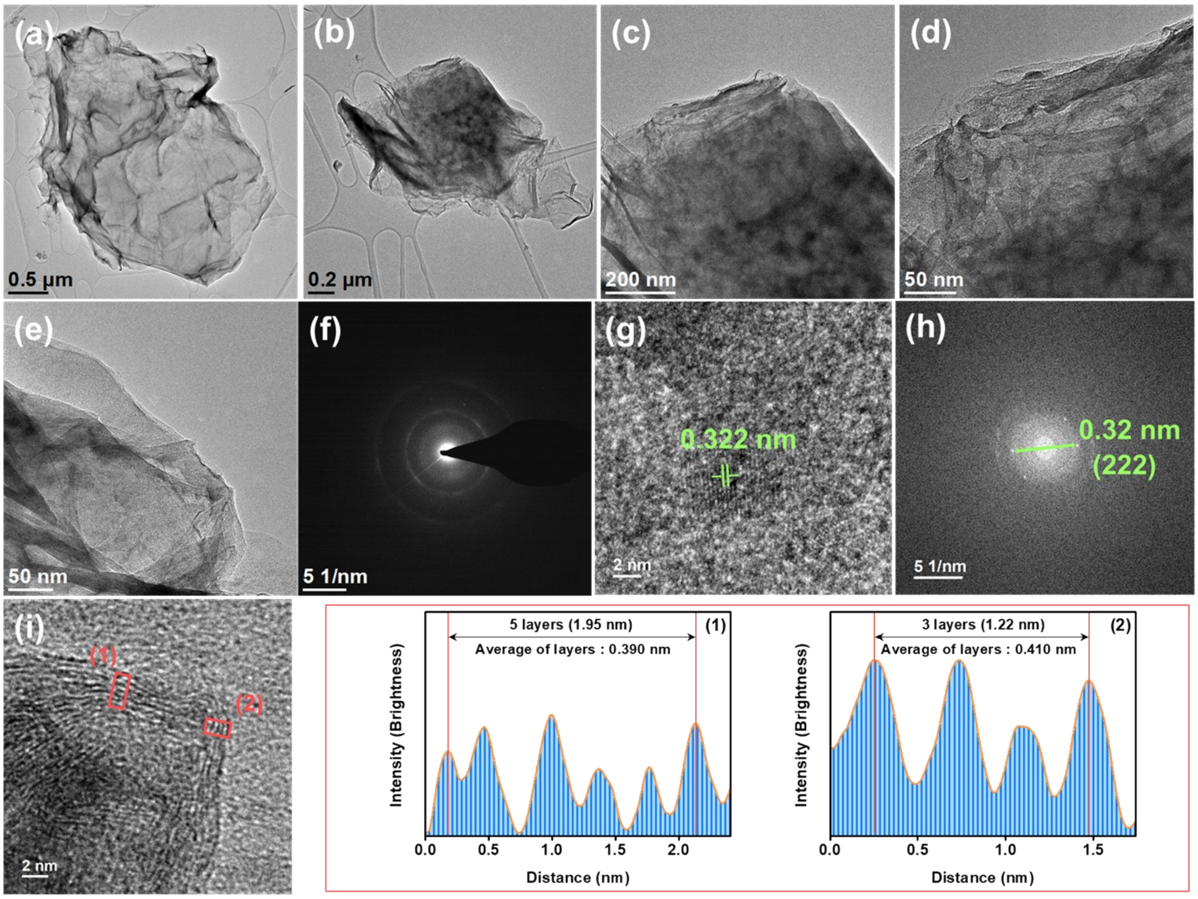

Fig. S10. (HR)TEM images of MrGO/Sb_2O_3 with the corresponding brightness profile and FFT images.

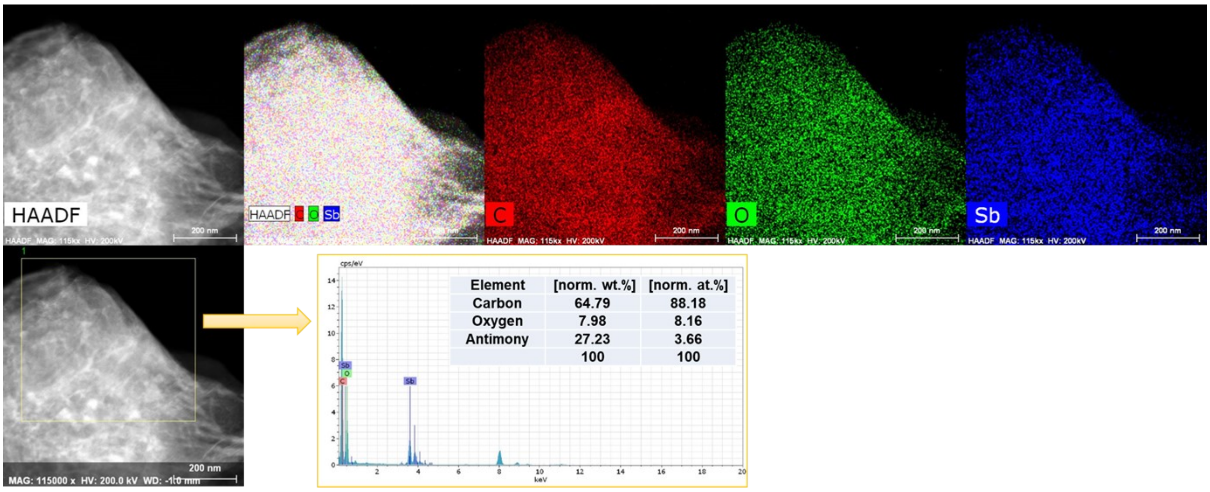

Element	[norm. wt.%]	[norm. at.%]
Carbon	64.79	88.18
Oxygen	7.98	8.16
Antimony	27.23	3.66
	100	100

Fig. S11. HAADF-STEM images and the corresponding EDS mapping for MrGO/Sb_2O_3.

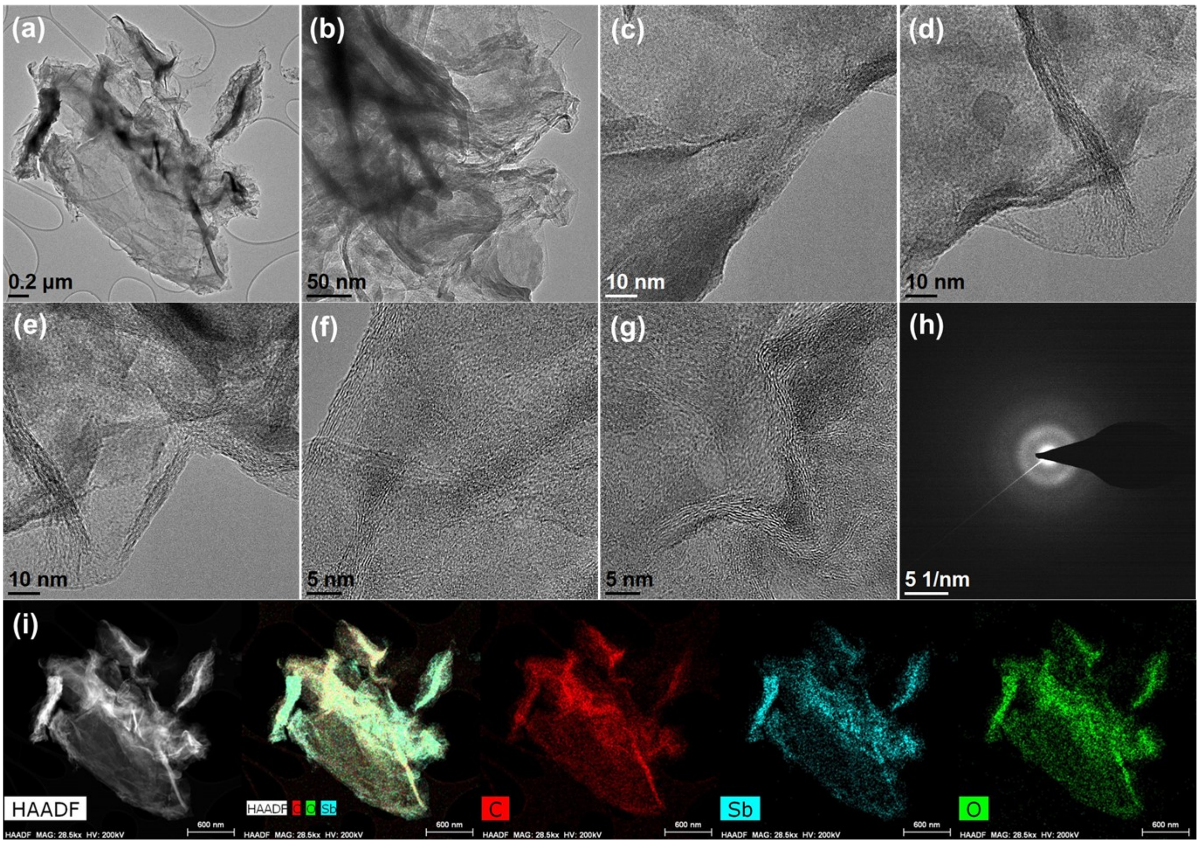

Fig. S12. (HR)TEM and HAADF-STEM images of PL-MrGO/$Li_xSb_2O_3$ with the corresponding brightness profile, FFT images and EDS mapping.

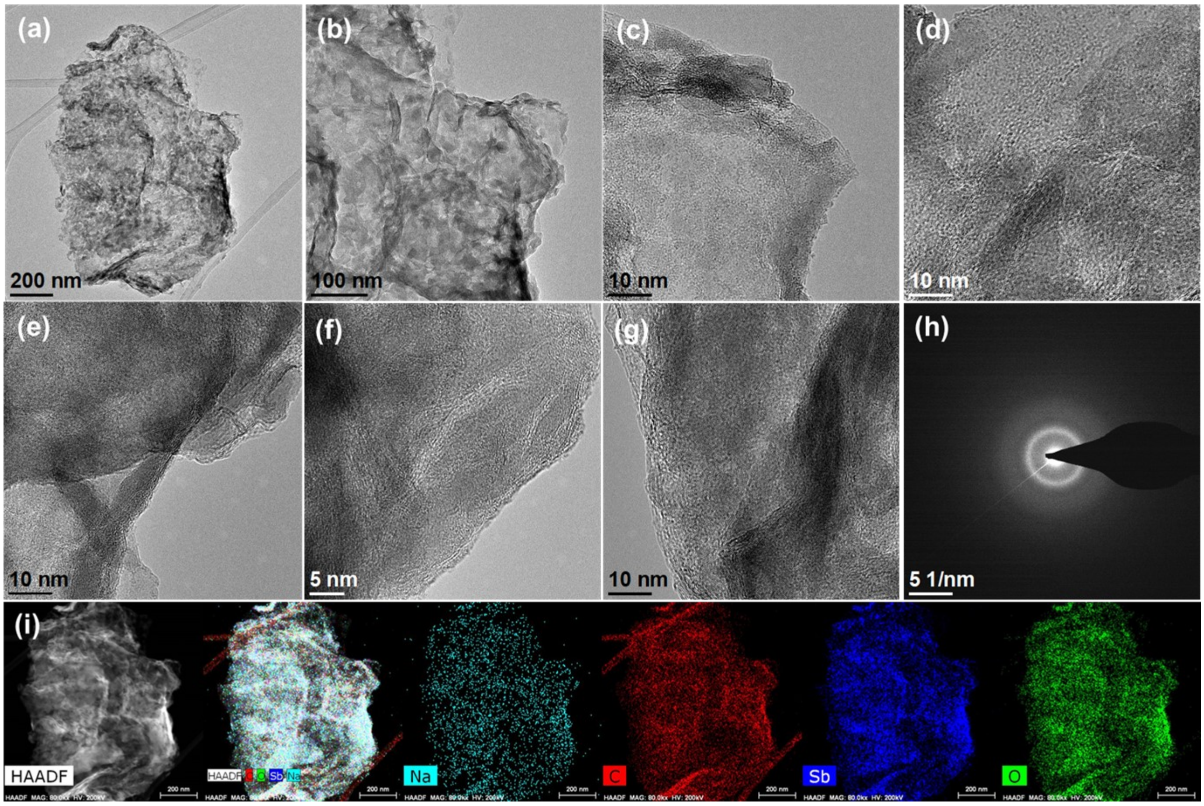

Fig. S13. (HR)TEM and HAADF-STEM images of PS-MrGO/$Na_xSb_2O_3$ with the corresponding brightness profile, FFT images and EDS mapping .

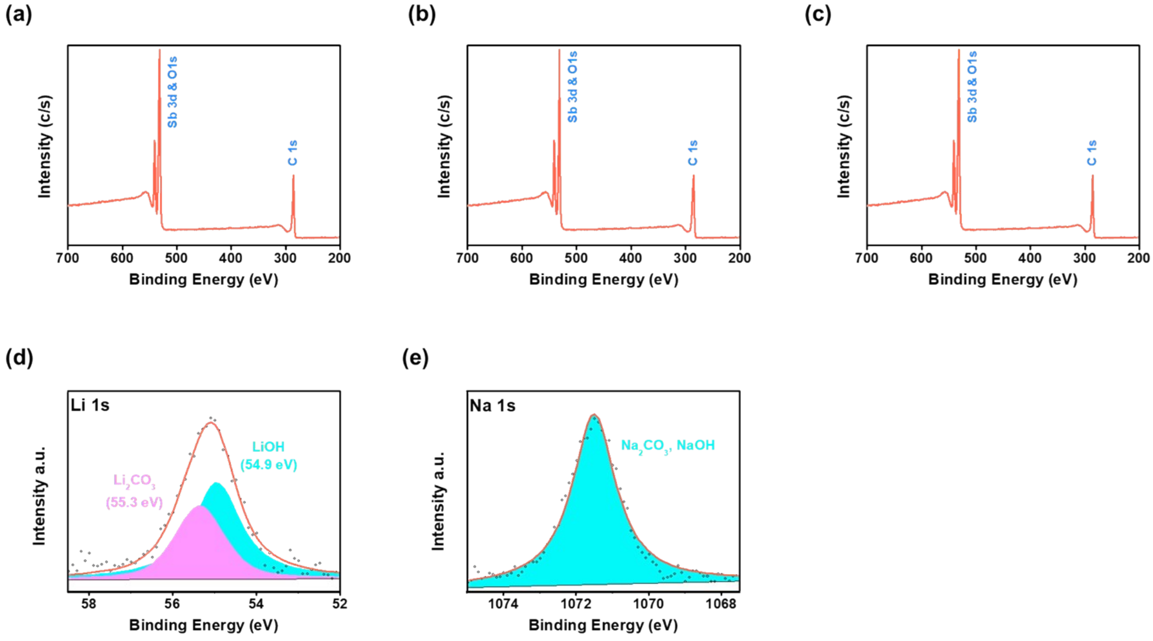

Fig. S14. XPS survey spectra of (a) MrGO/Sb_2O_3, (b) PL-MrGO/$Li_xSb_2O_3$, and (c) PS-MrGO/$Na_xSb_2O_3$; High-resolution XPS spectra of (d) Li 1s in PL-MrGO/$Li_xSb_2O_3$, (e) Na 1s in PS-MrGO/$Na_xSb_2O_3$.

Table S3. Elemental analysis of PL-MrGO/$Li_xSb_2O_3$.

XPS (wt%)			
C	**O**	**Sb**	**Li**
35.12	31.38	19.26	14.24

Table S4. Elemental analysis of PS-MrGO/$Na_xSb_2O_3$.

XPS (wt%)			
C	**O**	**Sb**	**Na**
51.14	12.86	32.06	3.9

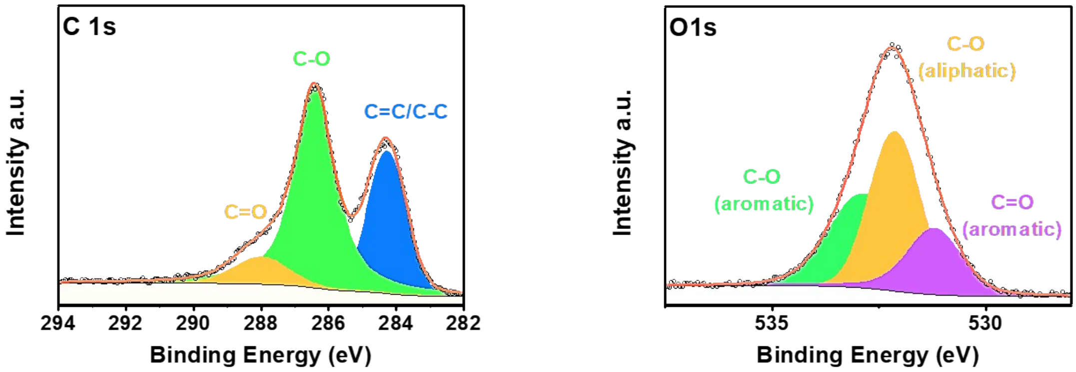

Fig. S15. High-resolution XPS spectra of Li 1s and O 1s in GO

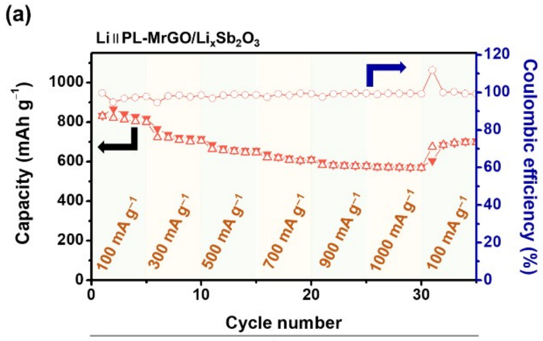

Current density (mA g^{-1})	Capacity retention (%)
300	82.6
500	75.8
700	70.6
900	67.0
1,000	66.2

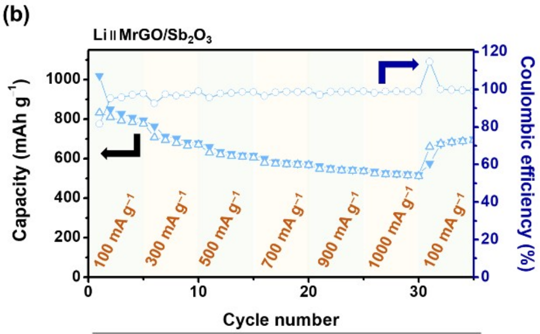

Current density (mA g^{-1})	Capacity retention (%)
300	79.8
500	72.4
700	67.4
900	63.6
1,000	60.9

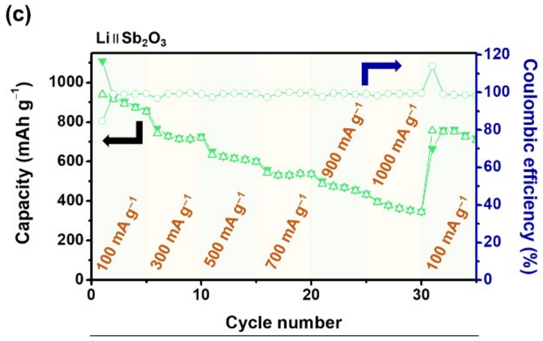

Current density (mA g^{-1})	Capacity retention (%)
300	78.6
500	65.3
700	58.3
900	47.3
1,000	37.6

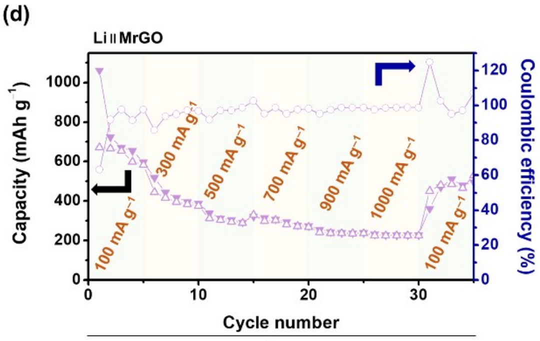

Current density (mA g^{-1})	Capacity retention (%)
300	53.6
500	44.6
700	37.8
900	33.1
1,000	31.2

Fig. S16. Rate performance and capacity retention at various current densities for the (a) PL-MrGO/Li$_x$Sb$_2$O$_3$, (b) MrGO/Sb$_2$O$_3$, (c) Sb$_2$O$_3$ and (d) MrGO electrodes over the initial 35 cycles, as shown in Fig. 4a. Capacity retention at current densities of 300, 500, 700, 900, and 1000 mA g^{-1} was calculated relative to the reversible capacity (discharge capacity in the 2nd cycle) measured at 100 mA g^{-1}.

Table S5. Performance metrics of Sb-based anode materials for LIBs reported in the last three years; [a] capacity (mA h g^{-1}); [b] current density (mA g^{-1}).

Anode materials	**Brief description**	**Capacity (Capacity[a]/Current density[b]/Cycle number)**	**Voltage range (vs. Li/Li$^+$)**	**Ref.**
PL-MrGO/Li$_x$Sb$_2$O$_3$	-Pre-lithiated MrGO/Li$_x$Sb$_2$O$_3$ combines a stable inorganic SEI and amorphous Li$_x$Sb$_2$O$_3$, achieving high coulombic efficiency and excellent cycling stability in LIBs.	877.7/100/150 715.7/1000/1000 315.3/5000/300	0.01–3.0 V	**This work**
MrGO/Sb$_2$O$_3$	-MrGO/Sb$_2$O$_3$ integrates Sb$_2$O$_3$ nanoparticles into a graphene matrix, enhancing conductivity and mitigating volume changes for stable energy storage.	736.4/100/150 335.5/1000/1000 169.4/5000/3000		
Sb@HPC	Sb@HPCs were synthesized by encapsulating Sb nanoparticles in a hierarchical porous carbon structure to improve electrochemical performance.	595.2/100/100 320.4/1000/800	0.01–3.0 V	S1
SbBr$_3$	SbBr$_3$ was used as an anode, where a two-step lithiation process creates a porous Sb structure.	345/100/100	0.01–2.0 V	S2
NSO-CB	Nickel antimony oxide (NiSb$_2$O$_6$; NSO) is synthesized via co-precipitation. The tri-rutile phase of NSO stores lithium ions via a conversion mechanism.	574/500/100	0.01–2.5 V	S3
DCAS	Crystalline organic hybrid cadmium antimony sulfide (DCAS) nanoparticles were synthesized via solvothermal synthesis, ball milling, and ultrasonic pulverization.	705.6/1000/500	0.01–3.0 V	S4
NiSb@CN	M-Sb (M=Co, Ni) nanoparticles in nitrogen-doped carbon nanofibers form 3D composites that reduce volume expansion and improve charge transport.	647.4/500/600	0.01–3.0 V	S5
Sb/CoSb$_2$@CN		620.2/500/600		
amorphous Sb/C-40	The amorphous Sb/C electrode, prepared via high-energy ball milling, demonstrates outstanding cycling stability by mitigating volume expansion and enhancing diffusion kinetics.	407.3/2000/1500	0.01–2.0 V	S6
C-Sb-2	C-Sb composites were synthesized via electrospinning, embedding Sb in amorphous carbon fibers to improve conductivity and stability	589.2/500/1000	0.01–3.0 V	S7
Si–Sb	The Si–Sb composite was synthesized via magnesiothermic reduction and chemical etching to create a porous structure with Sb nanodots.	820/1000/320	0.01–1.5 V	S8
MXene@AME	The MXene@AME heterostructure was synthesized via	455/200/300	0.01–3.0	S9

	electrostatic self-assembly, surface grafting, and annealing to form Ti−O−Sb bonds.	463/1000/2000	V	
Sb_6O_{13}/HrGO	Sb_6O_{13} was embedded in 3D HrGO sheets via an H_2O_2-assisted solvothermal method.	725.1/200/200	0.01–3.0 V	S10
MSC-2	The MXene-reinforced Sb@C nanocomposite was synthesized by combining MXene with a MOF-derived carbon layer.	230.4/2000/1000	0.01–3.0 V	S11
Sb_2O_3-rGO	Sb_2O_3-rGO composites were developed to address the volume expansion issue of Sb_2O_3.	744/100/310 386.9/500/1200	0.01–3.0 V	S12
SS-GO	Sb nanoparticles were encapsulated in carbon spheres and connected with graphene via a hierarchical double-carbon composite strategy.	373.7/2000/2200	0.01–2.5 V	S13
Sb_2S_3/SnO_2@rGO	Sb_2S_3/SnO_2@rGO composite was synthesized by anchoring Sb_2S_3/SnO_2 quantum dots on rGO, enhancing conductivity and stability through a p–n heterojunction.	474/3000/2000	0.01–3.0 V	S14
$CoSb_2O_6$/rGO	The $CoSb_2O_6$/rGO composite was synthesized using a sol–gel method, with rGO added to buffer volume expansion and enhance ion/electron transfer.	444.8/1000/100	0.01–3.0 V	S15
ZSO-CB	Zinc antimony oxide ($ZnSb_2O_6$) was synthesized by a solution-based method, and ZSO-CB electrodes were fabricated using electrophoretic deposition at 100 V for 3 minutes.	464/500/400	0.01–3.0 V	S16
3:1 TiO_2/Sb_2O_3 composite	TiO_2@Sb_2O_3 composites were synthesized by combining TiO_2 and Sb_2O_3 in different ratios through a straightforward method.	536/100/100	0.01–3.0 V	S17
Co–Sb_2O_5/rGO	Co–Sb_2O_5/rGO nanocomposite was synthesized via solvothermal method, with Co^{2+} ions enhancing Sb_2O_5 deposition on rGO, improving electron/ion migration and stability.	1027/200/200 648/500/500	0.01–3.0 V	S18
NS-C@$SbPO_4$/MoO_x	NS-C@$SbPO_4$/MoO_x nanowires were synthesized by annealing polyphosphazene-coated Sb_2MoO_6, forming N/S co-doped carbon shells to enhance conductivity and stability.	449.8/1000/700	0.01–3.0 V	S19
Sb-Si-Te@C	$Sb_2Si_2Te_6$ was synthesized by mechanical alloying and annealing, then coated with carbon via PAN pyrolysis to improve conductivity and cycling stability for LIB anodes.	505.6/100/200	0.01–2.5 V	S20
Sb_2O_3/rGO-100	The Sb_2O_3/rGO composite was made by thermally decomposing antimony 2-ethylhexanoate on rGO, forming ultrafine Sb_2O_3 nanoparticles.	513/500/300	0.01–3.0 V	S21
NiSb/C	NiSb alloy embedded in nitrogen-doped carbon (NiSb/C) was synthesized using citric acid as a surfactant, creating a carbon layer with high defects and uniform NiSb nanoparticle	426/2000/450	0.01–2.6 V	S22

	dispersion.			
NiSb-C	NiMC alloys (M: Sb, Sn) were synthesized by template and substitution reactions, anchoring nanoscale particles in hollow N-doped carbon tubes.	1259/100/100 559/2000/800	0.01–3.0 V	S23
Sb@C	The Sb@C anode was synthesized using the Stöber sol-gel method with resorcinol-formaldehyde resin, CTAB stabilization, and pH variation, forming a mesoporous carbon coating on Sb.	536/100/200	0.01–2.5 V	S24
Sb_2S_3@0.3CDs	Sb_2S_3@Sb@C composite was synthesized by one-step heat treatment of stibnite and carbon dots.	648.1/100/100 587.7/500/200	0.01–3.0 V	S25
Sb_2S_3/Sb@TiO_2@C	The Sb_2S_3/Sb@TiO_2@C composite was synthesized by coating Sb_2S_3 nanorods with TiO_2 and polydopamine, followed by carbothermic reduction, creating a core–shell–shell structure.	495.8/500/500	0.01–3.0 V	S26
TAO@G	TAO@G was synthesized through a hydrothermal process, combining TAO nanoparticles with graphene to improve electrical conductivity and mitigate volume expansion.	648.1/500/365	0.01–3.0 V	S27
S@Sb@N-CNF	The S@Sb@N-CNFs were synthesized by preparing an antimony and sulfur precursor in nitrogen-doped electrospun carbon nanofibers, followed by carbonization to embed Sb nanoparticles within the doped carbon matrix.	394.5/2000/2000 288.5/5000/5000	0.01–3.0 V	S28
3DPNS-Sb/C-2	The 3DPNS-Sb/C composites were synthesized by embedding Sb nanoparticles in a self-supported organic carbon 3D polymer network via a hydrothermal reaction followed by heat treatment, ensuring uniformity and structural integrity.	440.5/1000/250	0.01–2.0 V	S29
Sb@C@NC	The spindle-structured Sb@C@NC anode was fabricated using a metal–organic-framework-derived approach, followed by polydopamine coating and galvanic replacement, which effectively reduces volume expansion and improves electrochemical stability.	160/1000/500	0.01–2.0 V	S30
Sb/N-HPCNF	Sb/N-HPCNF was synthesized through electrospinning and in-situ substitution to create a hollow structure that enhances electrochemical performance and cycling stability for sodium-ion battery applications.	281/2000/2000	0.01–2.5 V	S31
Sb_2S_3-NPs@AC	Sb_2S_3 nanoparticles were encapsulated in activated carbon as anode materials for lithium-ion batteries using a high-temperature melting method with untreated natural stibnite ore.	326.3/300/800	0.01–3.0 V	S32
Sb_2O_4@PPy nanocomposite	Sb_2O_4@PPy core-shell nanospheres were synthesized using a method combining controllable nanostructure synthesis and conductive composite engineering.	542.8/1000/250	0.01–3.0 V	S33

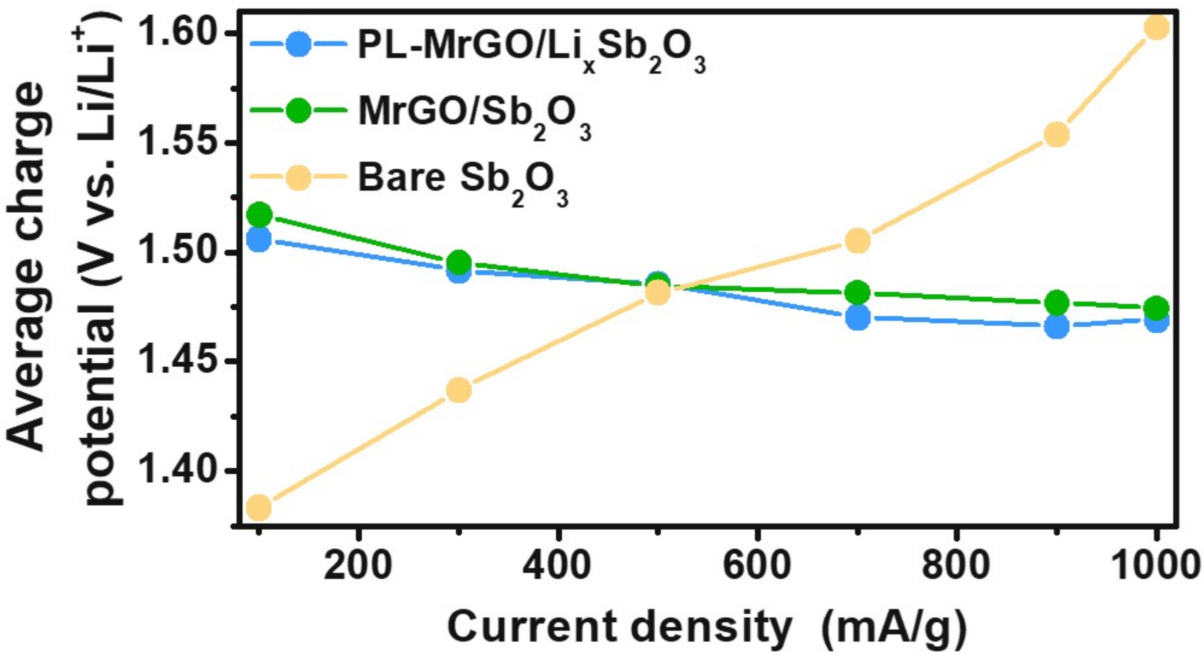

Fig. S17. Average charge potential of PL-MrGO/Li$_x$Sb$_2$O$_3$, MrGO/Sb$_2$O$_3$, and bare Sb$_2$O$_3$ at different current densities (100−1000 mA g^{-1}).

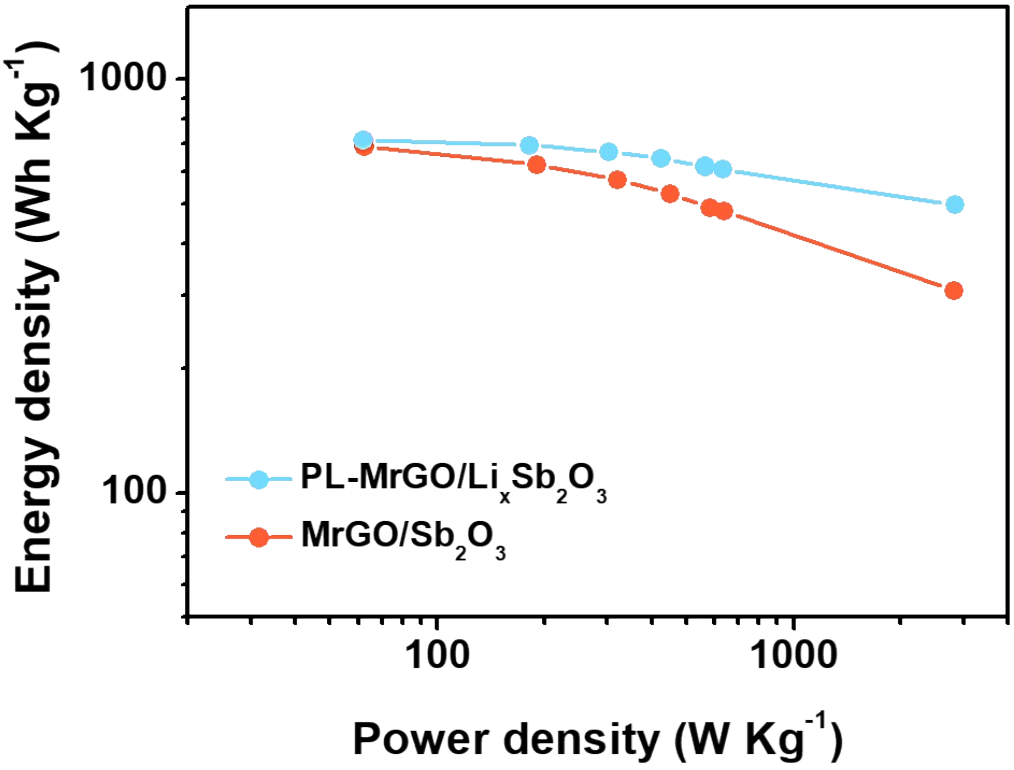

Fig. S18. Ragone plots of PL-MrGO/Li$_x$Sb$_2$O$_3$ and MrGO/Sb$_2$O$_3$ electrodes in LIBs.

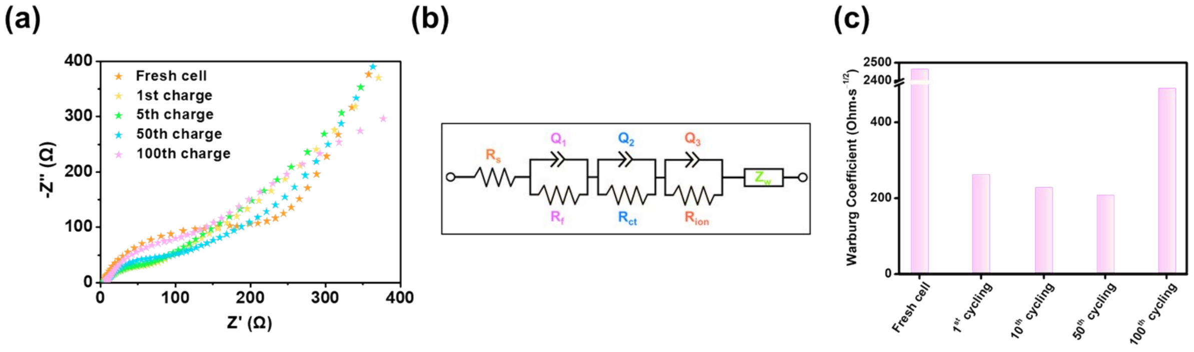

Fig. S19. (a) Nyquist plot and (b) DRT plot of the bare Sb_2O_3 electrode in LIBs measured up to the 100th cycle; (c) Warburg coefficients

Table S6. Impedance parameters fitted using the equivalent circuit model in **Fig. 6g**; R_s (Ω); R_f (Ω); R_{ct} (Ω); R_{ion} (Ω).

	MrGO/Sb_2O_3			**PL-MrGO/$Li_xSb_2O_3$**		
	R_s	**R_f**	**R_{ct}**	**R_s**	**R_f**	**R_{ct}**
Fresh cell	3.3	8.2	117.4	4.5	5.6	59.2
1st cycle	3.5	7.2	20.3	4.1	4.8	22.5
5th cycle	3.8	8.4	21.7	4.5	5.0	24.1
50th cycle	6.9	9.3	26.9	3.4	3.9	20.4
100th cycle	4.5	8.7	25.0	3.8	3.7	18.7

	MrGO			**bare Sb_2O_3**			
	R_s	**R_f**	**R_{ct}**	**R_s**	**R_f**	**R_{ct}**	**R_{ion}**
Fresh cell	4.9	10.8	73.5	5.5	19.4	168.7	85.1
1st cycle	4.5	14.2	21.6	4.6	22.3	88.5	41.8
5th cycle	5.6	13.6	20.8	4.8	19.6	82.9	33.6
50th cycle	4.7	14.5	28.4	6.2	28.1	104.8	61.5
100th cycle	3.8	13.2	26.1	7.2	42.9	126.3	93.5

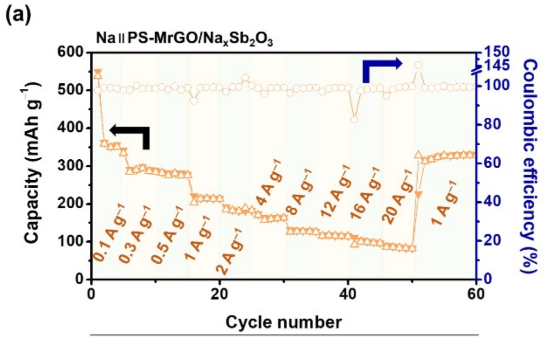

Current density (A g^{-1})	Capacity retention (%)
0.3	82.6
0.5	80.6
1	62.8
2	54.6
4	49.1
8	37.4
12	33.9
16	31.9
20	25.8

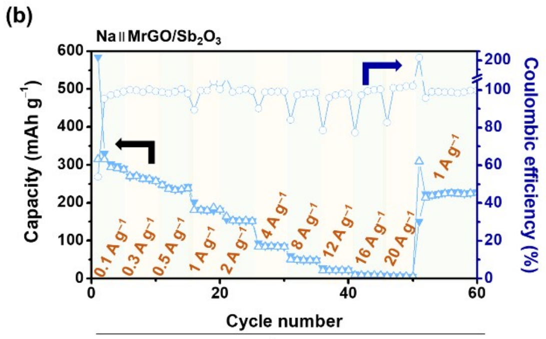

Current density (A g^{-1})	Capacity retention (%)
0.3	81.9
0.5	75.8
1	61.3
2	47.3
4	28.3
8	18.2
12	8.3
16	3.6
20	2.4

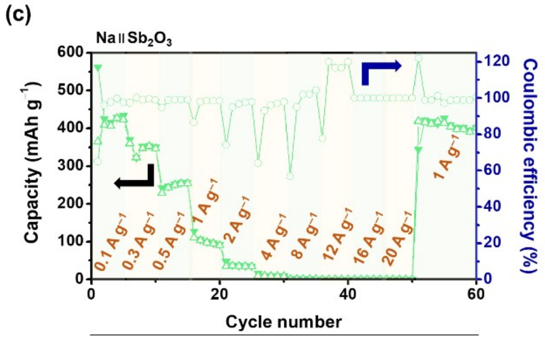

Current density (A g^{-1})	Capacity retention (%)
0.3	80.6
0.5	57.0
1	30.1
2	11.3
4	3.6
8	0.6
12	< 0.1
16	< 0.1
20	< 0.1

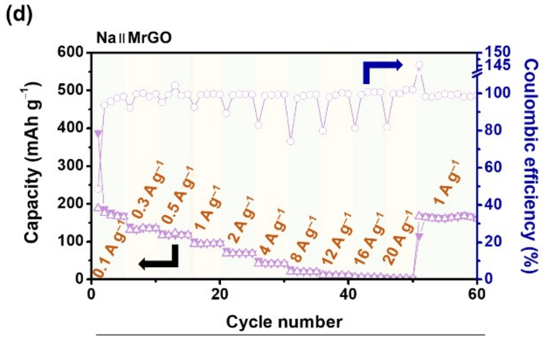

Current density (A g^{-1})	Capacity retention (%)
0.3	75.8
0.5	65.7
1	53.9
2	41.1
4	26.9
8	14.7
12	7.8
16	3.3
20	2.1

Fig. S20. Rate performance and capacity retention at various current densities for the (a) PS-MrGO/Na$_x$Sb$_2$O$_3$, (b) MrGO/Sb$_2$O$_3$, (c) Sb$_2$O$_3$ and (d) MrGO electrodes over the initial 35 cycles, as shown in Fig. 4a. Capacity retention at current densities of 0.1, 0.3, 0.5, 1, 2, 4, 8, 12, 16 and, 20 A g^{-1} was calculated relative to the reversible capacity (discharge capacity in the 2nd cycle) measured at 0.1 A g^{-1}.

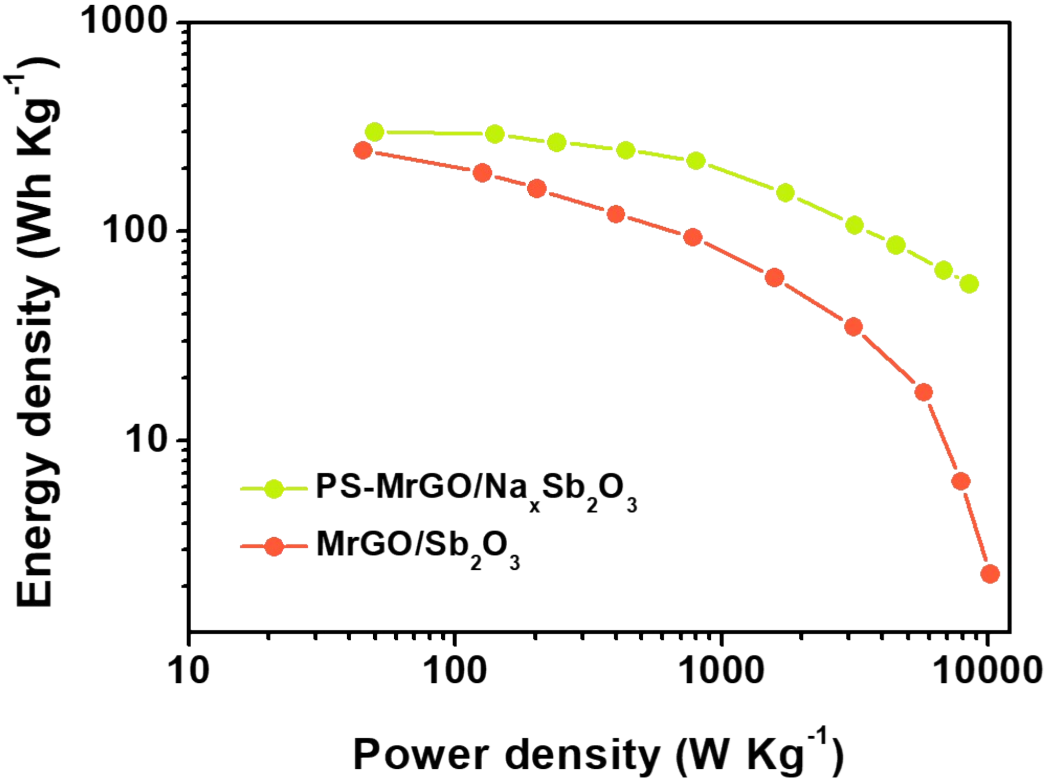

Fig. S21. Ragone plots of PS-MrGO/Na$_x$Sb$_2$O$_3$ and MrGO/Sb$_2$O$_3$ electrodes in SIBs.

Table S7. Performance metrics of Sb-based anode materials for SIBs reported in the last two years; $^{a)}$ capacity (mA h g^{-1}); $^{b)}$ current density (mA g^{-1}).

Anode materials	**Brief description**	**Capacity (Capacity$^{a)}$/Current density$^{b)}$/Cycle number)**	**Voltage range (vs. Na/Na$^+$)**	**Ref.**
PS-MrGO/Na$_x$Sb$_2$O$_3$	Pre-sodiated PS-MrGO/Na$_x$Sb$_2$O$_3$ features amorphous Na$_x$Sb$_2$O$_3$ and a robust SEI layer, offering superior cycling stability and rate performance in SIBs.	386.2/100/300 313.1/1200/3000	0.01–2.5 V	**This work**
MrGO/Sb$_2$O$_3$		251.7/100/300 149.8/1200/3000		
Sb SA/PC-2	The Sb SA/PC composite was synthesized by introducing carbon vacancies into a carbon matrix, which facilitated the anchoring of Sb single atoms.	364.4/5000/5000	0.01–2.5 V	S34
Sb@3D-Cu	The Sb@3D-Cu anode was synthesized using FDM 3D printing, sintering, and electrodeposition.	289.6/1000/200	0.01–2.0 V	S35
Co–Sb$_2$O$_5$/rGO	The Sb$_2$O$_5$/rGO composite was synthesized by using Co^{2+} ions to anchor Sb$_2$O$_5$ nanoparticles onto rGO sheets, forming CoSb$_2$O$_6$ nucleation sites.	352.3/100/100	0.01–3.0 V	S18
SS-GO	Sb nanoparticles were encapsulated in carbon spheres and connected with graphene via a hierarchical double-carbon composite strategy.	350/1000/120	0.01–2.5 V	S13
SNbM-2	Tin-antimony/carbon porous fibers were synthesized by electrospinning and heat treatment, improving ion transport and reducing volume expansion for better battery performance.	319.5/100/100	0.01–3.0 V	S36
ZSO/rGO	The ZSO/rGO hybrid nanocomposite was synthesized by combining zinc antimony oxide (ZSO) with reduced graphene oxide (rGO).	357.21/50/150	0.01–3.0 V	S37
Sb/Sb$_4$O$_5$Cl$_2$/C	The Sb/Sb$_4$O$_5$Cl$_2$/C composite was synthesized through heat treatment, combining Sb precursors, a carbon source, and controlled conditions.	508.5/100/100	0.01–2.5 V	S38
Bi$_{44.9}$Sb$_{55.1}$	The Bi-Sb alloy anode was synthesized using pulsed electrodeposition, forming a Bi$_{44.9}$Sb$_{55.1}$ structure. This design optimizes ion and electron transport.	494.7/1000/50	0.01–1.5 V	S39
FSG-200	FeSbO$_4$-Sb$_2$O$_4$/rGO composite was synthesized using a solvothermal method, anchoring hetero-nanocrystals on rGO to improve conductivity and ion diffusion.	204/500/1050	0.01–3.0 V	S40

m-Sb/C@MXene	The m-Sb/C@MXene composite is synthesized by embedding micro-sized Sb particles in carbon, then integrating them with a $Ti_3C_2T_x$ MXene network.	407.1/100/100 285.8/500/200	0.01–2.0 V	S41
$Sb@Sb_2O_3@C$	The core-shell $Sb@Sb_2O_3$ heterostructure encapsulated in porous carbon was synthesized using a NaCl template-assisted freeze-drying method combined with slow oxidation.	440.6/5000/5000	0.01–3.0 V	S42
Sb ACs@NSC	The Sb atomic clusters@N, S co-doped carbon networks were synthesized via an in situ vaporization-reduction method to balance ultra-small Sb clusters with high loading in the composite.	306.7/10000/1000	0.01–3.0 V	S43
$Sn/Sb@Sb_2SnO_5@P$ CFs-N	The $Sn/Sb@Sb_2SnO_5@PCFs$-N composite was synthesized using electrostatic spinning, where Sn and Sb nanocrystals were in situ generated around Sn-Sb oxide.	450/50/100	0.01–1.5 V	S44
$Sb/Sb_2O_3@NPC$-1.0	The $Sb/Sb_2O_3@NPC$ anode was synthesized using a gas–solid dual template method, embedding Sb/Sb_2O_3 nanoparticles in nitrogen-doped porous carbon.	300.3/1000/1000	0.01–3.0 V	S45
$Sb_2Se_3@N$-CQDs/CNF	The $Sb_2Se_3@N$-CQDs/CNF was synthesized by combining Sb_2Se_3 nanorods, nitrogen-doped carbon quantum dots, and carbon nanofibers.	413.6/200/100	0.01–2.5 V	S46
Sb: HC-1:1	The Sb: HC-1:1 composite was made by mixing antimony oxychloride/oxide with hard carbon, forming interconnected carbon spheres with rod-shaped antimony oxychloride/oxide.	332/200/100	0.01–2.5 V	S47
BiSb-Se/CNF	The BiSb-Se/CNFs composite anode was synthesized by integrating selenium-doped carbon nanofibers with bismuth-antimony alloy nanocrystals.	370/500/650 309/2000/2000	0.01–3.0 V	S48
mSb/Sb_2O_3-HCl	The mSb/Sb_2O_3-HCl composite was synthesized by reducing $SbCl_3$ with NaK alloy, followed by treatment with an HCl solution.	456/800/100	0.01–2.0 V	S49
$Bi_{0.4}Sb_{0.6}$	The BiSb alloy nanosheets were synthesized by using metallic Bi as a scaffold, forming a 2D alloy with different Bi/Sb ratios.	377/100/100	0.01–2.0 V	S50
Sb/Sb_2O_3-200	Sb/Sb_2O_3 nanoparticles were synthesized by oxidizing Sb nanoparticles in air at 200 °C, optimizing the Sb_2O_3:Sb ratio and particle size for improved Na^+ storage and reduced stress in sodium-ion batteries.	540/100/100	0.01–2.0 V V	S51
$SbPO_{4-x}@CNFs$	The $SbPO_{4-x}@CNFs$ composite was synthesized by integrating $SbPO_4$ precursors with carbon nanofibers and inducing oxygen vacancy defects to enhance conductivity and stability.	322.9/500/200	0.01-1.5 V	S52
Sb@Void@GDY NB	Sb@Void@GDY nanoboxes were synthesized by coating Sb	593/100/200	0.01–2.0	S53

	nanoparticles with polydopamine, converting it into GDY shells via chemical vapor deposition, and creating voids between Sb and GDY to form a yolk–shell structure.	325/1000/8000	V	
SnSb@CNF/CNT	The SnSb@CNF/CNT anode was synthesized using electrospinning and calcination, featuring a 3D cross-linked carbon nanofiber (CNF) and carbon nanotube (CNT) structure.	210/500/700	0.01–3.0 V	S54
Bi_1Sb_1@C	A series of Bi–Sb composites confined in a porous carbon matrix were synthesized via pyrolysis.	201.9/200/500 167.2/1000/8000	0.01–2.0 V	S55
TiO_2@C-Sb	TiO_2@C-Sb nanotablets were synthesized by absorbing $SbCl_3$ into a TiO_2@C matrix and calcining the mixture.	219/500/1000	0.01–3.0 V	S56
Sb-N-C	Antimony-doped hard carbon materials were synthesized by anchoring Sb atoms on nitrogen-doped carbon.	254/1000/2000	0.01–3.0 V	S57
$Ti_3C_2T_x/Sb_2Se_3$	The $Sb_2Se_3/Ti_3C_2T_x$ film was synthesized using electrostatic self-assembly, where the $Ti_3C_2T_x$ MXene nanosheets interacted with the Sb_2Se_3 nanowires to enhance the electrochemical performance.	568.9/100/100 304.1/1000/500	0.01–2.5 V	S58
Sb@CN	Sb nanoparticles encapsulated in hollow mesoporous N-doped carbon spherical shells were successfully synthesized using a SiO_2 template.	282/660/5000	0.01–3.0 V	S59
Sb_2S_3/S@S-doped C	The Sb_2S_3/S@S-doped carbon composite with a hollow core-shell structure was synthesized using a template method combined with a complexation reaction.	479/2000/100	0.01–3.0 V	S60
$FeSb_2S_4$/Sb/rGO	$FeSb_2S_4$/Sb/rGO composite was synthesized by combining $FeSb_2S_4$ with Sb and rGO, then forming 3D discs using CNTs and rGO for conductivity.	252.7/1000/100	0.01–2.5 V	S61
NF–Sb_2S_3@rGO	Sb_2S_3@rGO hybrid was synthesized through a hydrothermal method, creating a 3D Sb_2S_3 nanoflower structure coated with reduced graphene oxide (rGO).	459/100/200	0.01–2.5 V	S62
MoS_2@Sb_2S_3/rGO	The MoS_2@Sb_2S_3/rGO composites were prepared by combining MoS_2 and Sb_2S_3 in a heterostructure and wrapping them with 3D interconnected rGO networks.	162.1/5000/1100	0.01–3.0 V	S63

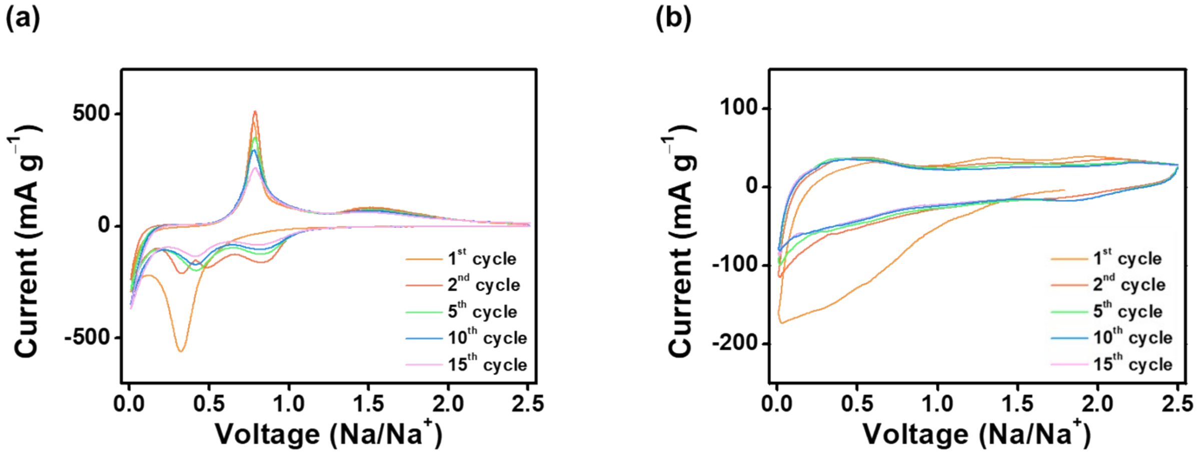

Fig. S22. CV profiles of (a) the bare Sb_2O_3 and (b) MrGO electrodes at a scan rate of 0.1 mV s^{-1}.

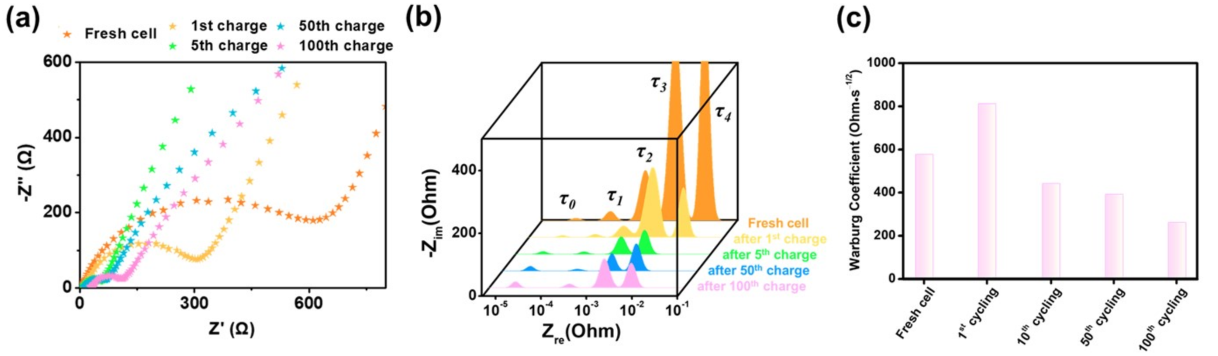

Fig. S23. (a) Nyquist plot and (b) DRT plot of the bare Sb_2O_3 electrode in SIBs measured up to the 100th cycle; (c) Warburg coefficients.

Table S8. Impedance parameters fitted using the equivalent circuit model in **Fig. 9g**; R_s (Ω); R_f (Ω); R_{ct} (Ω); R_{ion} (Ω).

	MrGO/Sb_2O_3				**PS-MrGO/$Na_xSb_2O_3$**			
	R_s	**R_f**	**R_{ct}**	**R_{ion}**	**R_s**	**R_f**	**R_{ct}**	**R_{ion}**
Fresh cell	7.8	24.5	175.1	-	5.7	22.9	120.5	-
1st cycle	8.9	28.8	180.6	-	4.6	16.6	108.1	-
5th cycle	8.7	30.4	155.8	-	6.2	19.4	92.3	-
50th cycle	11.1	27.3	156.7	-	8.5	14.8	88.7	-
100th cycle	10.5	24.8	89.6	-	6.6	13.2	84.8	-

	MrGO				**bare Sb_2O_3**			
	R_s	**R_f**	**R_{ct}**	**R_{ion}**	**R_s**	**R_f**	**R_{ct}**	**R_{ion}**
Fresh cell	10.2	32.9	305.3	199.6	6.7	28.2	342.8	251.6
1st cycle	12.3	34.2	238.6	94.1	13.8	56.5	230.9	88.4
5th cycle	11.6	38.7	207.3	-	6.2	152.5	165.7	-
50th cycle	13.8	38.9	183.8	-	8.9	87.9	137.6	-
100th cycle	13.6	41.5	172.6	-	26.2	85.1	151.0	-

Supplementary References

S1. Z. Li, Y. Gao, S. Xiong, S. Wang, L. Hou, J. Zhang and F. Gao, *J. Alloys Compd.*, 2024, **1002**, 175308.

S2. A. D. Singh, A. A. Cyril, A. Dey, G. Varshney and S. Sengupta, *J. Alloys Compd.*, 2024, **977**, 173305.

S3. U. Ray, D. Das, S. Jena, A. Mitra, K. Das, S. B. Majumder and S. Das, *J. Power Sources*, 2024, **594**, 234044.

S4. L. Zhai, H. Li, J. Wu, J. Luo, J.-M. Yu, Z. Pan, H. Li, B. Hu, B. Zheng and W.-W. Xiong, *ACS Appl. Mater. Interfaces*, 2024, **16**, 35024–35032.

S5. Z. Wu, H. Li, L. Fang, J. Li, W. Shi, T. Xu, X. Wang, L. Chang and P. Nie, *Electrochim. Acta*, 2024, **475**, 143613.

S6. Z.-Z. Yang, C.-Y. Zhang, Y.-Q. Ou, Z.-K. Su, Y. Zhao, H.-J. Cong, X.-P. Ai and J.-F. Qian, *Rare Metals*, 2024, **43**, 2039–2052.

S7. Y. Li, Y.-H. Zhao, L.-L. Zhao, P.-F. Wang, Y. Xie and T.-F. Yi, *Rare Metals*, 2024, **43**, 2994–3006.

S8. J.-G. Deng, H.-Q. Feng, Y.-L. Xu, S.-G. Guo, J.-P. Li, K.-F. Huo, J.-J. Fu, B. Gao and P.-K. Chu, *Rare Metals*, 2024, **43**, 4234–4242.

S9. Z. Bo, Z. Zheng, Y. Huang, P. Chen, J. Yan, K. Cen, R. Mo, H. Yang and K. (Ken) Ostrikov, *Chem. Eng. J.*, 2024, **485**, 149837.

S10. X. Zhou, X. Zheng, H. Lu, H. Deng, Z. Liu and J. Deng, *J. Energy Storage*, 2024, **92**, 111999.

S11. L. Feng, J. Chen, Y. Li, S. Zhou, R. A. Soomro, P. Zhang and B. Xu, *Chem. Eng. J.*, 2024, **489**, 151396.

S12. Y. Jin, H. Hwang, H. Seong, J. H. Moon, G. Kim, H. Yoo, T. Jung, J. B. Lee and J. Choi, *ACS Appl. Energy Mater.*, 2024, **7**, 2955–2962.

S13. Y. Xiang, X. Hu, X. Zhong, W. Deng, G. Zou, H. Hou and X. Ji, *Adv. Funct. Mater.*, 2024, **7**, 2311478.

S14. H. Yin, G. Zhan, R. Yan, X. Wu, Q. Hu and X. Huang, *Dalton Trans.*, 2024, **53**, 7142–7151.

S15. J. Chen, M. Tang, G. Wang, L. Liu, X. Hu, H. Liao and X. Hu, *Mater. Lett.*, 2024, **354**, 135346.

S16. U. Ray, D. Das, A. Mitra, S. B. Majumder and S. Das, *Mater. Lett.*, 2024, **355**, 135567.

S17. K. Gomez, E. Fletes, J. G. Parsons and M. Alcoutlabi, *Appl. Sci.*, 2024, **14**, 6598.

S18. X. Zhou, A. Wang, X. Zheng, D. Sun and Y. Yang, *Inorg. Chem. Front.*, 2024, **11**, 4167–4178.

S19. Q. Zhang, H. Wang, T. Yao, X. Lu, C. Li, Y. Qiu, P. Zhang, D. Wang, Y. Chen and L. Meng, *Small*, 2024, **20**, 2400468.

S20. J. Tang, L. Liu, J. Sun, Y. Ran, Y. Zheng, J. Chai, L. Wang and Z. Liu, *J. Alloys Compd.*, 2024, **989**, 174379.

S21. X. Chen, T. Yao, H. Dong, Q. Ge, S. Chen and Z. Ma, *Energy Fuels*, 2023, **37**, 5586–5594.

S22. M. Su, J. Li, K. He, K. Fu, P. Nui, Y. Chen, Y. Zhou, A. Dou, X. Hou and Y. Liu, *J. Colloid Interface Sci.*, 2023, **629**, 83–91.

S23. C. Weng, S. Huang, T. Lu, J. Li, J. Li, J. Li and L. Pan, *J. Colloid Interface Sci.*, 2023, **652**, 208–217.

S24. L. Dashairya, V. Chaturvedi, A. Kumar, T. R. Mohanta, M. Shelke and P. Saha, *Solid State Ion.*, 2023, **396**, 116243.

S25. Y. Xiang, L. Xu, L. Yang, Y. Ye, Z. Ge, J. Wu, W. Deng, G. Zou, H. Hou and X. Ji, *Nanomicro Lett.*, 2022, **14**, 136.

S26. Y. Zhang, S. Li, L. Liu, Y. Lin, S. Jiang, Y. Li, X. Ren, P. Zhang, L. Sun and H. Y. Yang, *ACS Appl. Mater. Interfaces*, 2022, **14**, 33064–33075.

S27. B. Xiao, G. Wu, T. Wang, Z. Wei, Y. Sui, B. Shen, J. Qi, F. Wei, Q. Meng, Y. Ren, X. Xue, J. Zheng, J. Mao, K. Dai and Q. Yan, *Ceram. Int.*, 2022, **48**, 2118–2123.

S28. Y. Mao, R. Chen, H. You, Y. Liu, S. Luan, L. Hou and F. Gao, *J. Alloys Compd.*, 2022, **904**, 164000.

S29. Z. Wang, F. Zeng, D. Zhang, Y. Shen, S. Wang, Y. Cheng, C. Li and L. Wang, *Nanomaterials*, 2022, **12**, 2322.

S30. J. Liu, P. Li, F. Li, Z. Liu, X. Xu and J. Liu, *Batteries*, 2022, **8**, 245.

S31. Y. Gu, R. C. Cui, G. Y. Wang, C. C. Yang and Q. Jiang, *Energy Technol.*, 2022, **10**, 2200746.

S32. Y. Du, F. Liu, L. Jiang, M. Jia and Z. Zhang, *J. Alloys Compd.*, 2022, **907**, 164469.

S33. L. Jiang, W. Yin, C. He, T. Luo, Y. Rui and B. Tang, *Colloids Surf. A Physicochem. Eng. Asp.*, 2022, **644**, 128843.

S34. W. Zhao, S. Lei, J. Li, F. Jiang, T. Wu, Y. Yang, W. Sun, X. Ji and P. Ge, *Adv. Energy Mater.*, 2024, **14**, 2304431.

S35. H. Gao, W. Gao and M. Pumera, *Adv. Funct. Mater.*, 2024, **34**, 2310563.

S36. X. Chen, Y. Huang, M. Zhang, Y. Yu, X. Li, D. Chen, J. Hong, S. Du and X. Guan, *Mater. Res. Express*, 2024, **11**, 035501.

S37. A. F. Hernández-Pascacio, R. E. Castellanos-Pineda, M. Laguna-Estrada and O. A. Jaramillo-Quintero, *Ceram. Int.*, 2024, **50**, 48183–48190.

S38. J. Płotek, A. Kulka, A. Maximenko, Ł. Kondracki, S. Trabesinger, M. Moździerz, P. Czaja and J. Molenda, *Energy Storage Mater.*, 2024, **72**, 103780.

S39. M. Chen, X. Han, X. Zheng, H. Shen, J. Wang, J. You, L. Yan, X. Meng, Q. Kang, Q. Wu, Y. Zhao and T. Ma, *Electrochim. Acta*, 2024, **478**, 143867.

S40. X. Zhou, A. Wang, X. Zheng, Z. Zhang, J. Song, H. Deng, P. Yan, D. Sun, Y. Yang and Z. Lei, *Appl. Surf. Sci.*, 2024, **648**, 159077.

S41. Y. Liang, Z. Wang, Z. Xu, S. Li, H. Luo, C. Xu and X. Cui, *Appl. Surf. Sci.*, 2024, **651**, 159234.

S42. Z. Yang, Y. Lu, R. Wang, X. Wang, X. Hao, Z. Zhu, L. Dai, M. Fan, T. Ma and Q. Kang, *Colloids Surf. A Physicochem. Eng. Asp.*, 2024, **694**, 134116.

S43. A. Xu, M. Huang, C. Liu, T. Li, X. Li, S. Wu, Z. Xu and Y. Yan, *Adv. Funct. Mater.*, 2024, **34**, 2400302.

S44. C. Yu, B. Liu, M. Li and X. Ding, *Ionics*, 2024, **30**, 1403–1412.

S45. G. Ma, C. Xu, D. Zhang, S. Che, Y. Wang, J. Yang, K. Chen, Y. Sun, S. Liu, J. Fu, Z. Zhou, Y. Qu, C. Ding and Y. Li, *J. Colloid Interface Sci.*, 2024, **673**, 26–36.

S46. C.-H. Wu, S. Kubendhiran, R.-J. Chung, C. Kongvarhodom, S. Husain, S. Yougbaré, H.-M. Chen, Y.-F. Wu and L.-Y. Lin, *J. Power Sources*, 2024, **623**, 235469.

S47. S. Ghosh, V. K. Kumar, S. Bhowmik and S. K. Martha, *J. Energy Storage*, 2024, **86**, 111090.

S48. X. Li, L. Zeng, W. Lai, Z. Lei, M. Ge, C. Fang, B. Weng, Q. Chen, M. Wei and Q. Qian, *Energy Fuels*, 2024, **38**, 16966–16975.

S49. T. Zhang, W. Zhang, D. Tang and Z. Zhao, *Inorg. Chem. Commun.*, 2024, **162**, 112159.

S50. Y. Liu, X. Liu, X. Wang, S. Ullah, Y. Peng, G. Pan, W. Gao, B. Song, X. Zhang, A. Jia, J. Wang, J. He and Y. Wu, *Adv. Funct. Mater.*, 2024, 2415092.

S51. J. Chen, S. Zhao, W. Meng, M. Guo, G. Wang, C. Guo, Z. Bai, Z. Li, J. Ye, H. Song and X. Wang, *Batteries*, 2023, **9**, 98.

S52. J. Wu, G. Wang, W. Zhang, L. Wang, J. Peng, Q. Li, Z. Liang, W. Fan, J. Wang and S. Huang, *J. Energy Chem.*, 2024, **90**, 110–119.

S53. Y. Liu, Y. Qing, B. Zhou, L. Wang, B. Pu, X. Zhou, Y. Wang, M. Zhang, J. Bai, Q. Tang and W. Yang, *ACS Nano*, 2023, **17**, 2431–2439.

S54. Z. Song, G. Wang, Y. Chen, Y. Lu and Z. Wen, *Chem. Eng. J.*, 2023, **463**, 142289.

S55. W. Ma, B. Yu, F. Tan, H. Gao and Z. Zhang, *Materials*, 2023, **16**, 2189.

S56. T. Yao, L. Li and H. Wang, *Chin. Chem. Lett.*, 2023, **34**, 108186.

S57. Y. Tong, Y. Wu, X. Liu, Z. Chen and H. Li, *J. Colloid Interface Sci.*, 2023, **648**, 575–584.

S58. J. Yang, J. Li, J. Lu, X. Sheng, Y. Liu, T. Wang and C. Wang, *J. Colloid Interface Sci.*, 2023, **649**, 234–244.

S59. Q. Mao, Y. Jia, W. Zhu and L. Gao, *J. Solid State Electrochem.*, 2023, **27**, 1433–1441.

S60. K. Li, L. Yue, J. Hu, X. Zhou, M. Xiao, C. Dai, C. Tian, Y. Yue, W. Zhang and J. Zhang, *Appl. Surf. Sci.*, 2023, **613**, 156111.

S61. D. Feng, S. Tang, H. Xu and T. Zeng, *J. Alloys Compd.*, 2023, **931**, 167576.

S62. J. Zhou, Y. Ding, Q. Dou, H. Li, R. Wang, D. Zhang and Y. Cao, *Mater. Chem. Phys.*, 2023, **303**, 127837.

S63. M. Zhu, J. Li, X. Yang, X. Li, L. Wang and W. Lü, *Appl. Surf. Sci.*, 2023, **624**, 157106.